Inorganic Chemistry

pubs.acs.org/IC

Article

Disruption of the Microtubule Network and Inhibition of VEGFR2 Phosphorylation by Cytotoxic *N,O*-Coordinated Pt(II) and Ru(II) Complexes of Trimethoxy Aniline-Based Schiff Bases

Sourav Acharya, Moumita Maji, Manas Pratim Chakraborty, Indira Bhattacharya, Rahul Das, Arnab Gupta, and Arindam Mukherjee*

Cite This: *Inorg. Chem.* 2021, 60, 3418−3430

Read Online

ACCESS | Metrics & More | Article Recommendations | Supporting Information

ABSTRACT: Platinum-based complexes are one of the most successful chemotherapeutic agents having a significant ground in cancer chemotherapy despite their side effects. During the past few decades, Ru(II) complexes have been emerging as efficient alternatives owing to their promising activities against platinum-resistant cancer. The pathway of action, lipophilicity, and cytotoxicity of a Pt or Ru complex may be tuned by varying the attached ligands, the coordination mode, and the leaving group. In this work, we report a family of Pt(II) and Ru(II) complexes (**1**−**5**) of three *N,O* and *N,N* donor-based trimethoxyanilines containing Schiff bases with the general formula $[Pt^{II}(L)(DMSO)Cl]$, $[Ru^{II}(L)(p\text{-cymene})Cl]$, $[Ru^{II}(L)(p\text{-cymene})Cl]^+$, and $[Pt^{II}(L)Cl_2]$. All of the complexes are characterized by different analytical techniques. ^1H NMR and electrospray ionization mass spectrometry (ESI-MS) data suggest that the *N,O*-coordinated Pt(II) complexes undergo slower aquation compared to the Ru(II) analogues. The change of the coordination mode to *N,N* causes the Ru complexes to be more inert to aquation. The *N,O*-coordinating complexes show superiority over *N,N*-coordinating complexes by displaying excellent *in vitro* antiproliferative activity against different aggressive cancer cells, *viz.*, triple-negative human metastatic breast adenocarcinoma MDA-MB-231, human pancreatic carcinoma MIA PaCa-2, and hepatocellular carcinoma Hep G2. *In vitro* cytotoxicity studies suggest that Pt(II) complexes are more effective than their corresponding Ru(II) analogues, and the most cytotoxic complex **3** is 10−15 times more toxic than the clinical drugs cisplatin and oxaliplatin against MDA-MB-231 cells. Cellular studies show that all of the *N,O*-coordinated complexes (**1**−**3**) initiate disruption of the microtubule network in MDA-MB-231 cells in a dose-dependent manner within 6 h of incubation and finally lead to the arrest of the cell cycle in the G2/M phase and render apoptotic cell death. The disruption of the microtubule network affects the agility of the cytoskeleton rendering inhibition of tyrosine phosphorylation of vascular endothelial growth factor receptor 2 (VEGFR2), a key step in angiogenesis. Complexes **1** and **2** inhibit VEGFR2 phosphorylation in a dose-dependent fashion. Among the Pt(II) and Ru(II) complexes, the former displays higher cytotoxicity, a stronger effect on the cytoskeleton, better VEGFR2 inhibition, and strong interaction with the model nucleobase 9-ethylguanine (9-EtG).

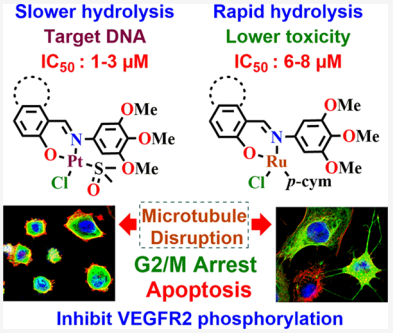

INTRODUCTION

Cancer is one of the leading causes of death globally, affecting billions of people every year.[1] The discovery of cisplatin by Rosenberg et al. opened up a new horizon for metal-based chemotherapeutics making Pt-based complexes a major choice in cancer chemotherapy. There are three Pt-based FDA-approved drugs, cisplatin, oxaliplatin, and carboplatin, used in clinics worldwide.[2] These Pt-based chemotherapeutics are effective against a wide range of cancers, *viz.*, testicular, ovarian, nonsmall cell lung, colon, prostate, cervical, breast, and stomach cancers.[3,4] The primary mechanism of action of these Pt-based chemotherapeutics is DNA crosslinking, which inhibits DNA from replicating further, causing cell cycle arrest and apoptosis.[2,5] Existing Pt drugs exhibit growing resistance toward various cancers, thereby increasing the demand for new Pt and non-Pt metal-based complexes with different mechanisms of action.[6−9] Ru and Ga are two other metals that show promising activity against cancer.[10−14] Ru(III/II) complexes have shown lower side effects and are active against Pt-resistant cancer.[15] Phase-I trial of Ru(III) analogue NKP 1339 (Figure 1) has been successfully completed. The mechanism of action suggests that the downregulation of the protein GRP78 by NKP 1339 may induce endoplasmic reticulum stress (ERS), leading to cell death.[16] Apart from this, Ru(II) derivatives also showed promising cytotoxicity, and recently, TLD1433, the first Ru(II) complex, (Figure 1) entered phase-I clinical trials

Received: December 30, 2020
Published: February 8, 2021

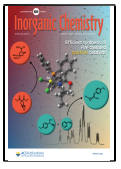

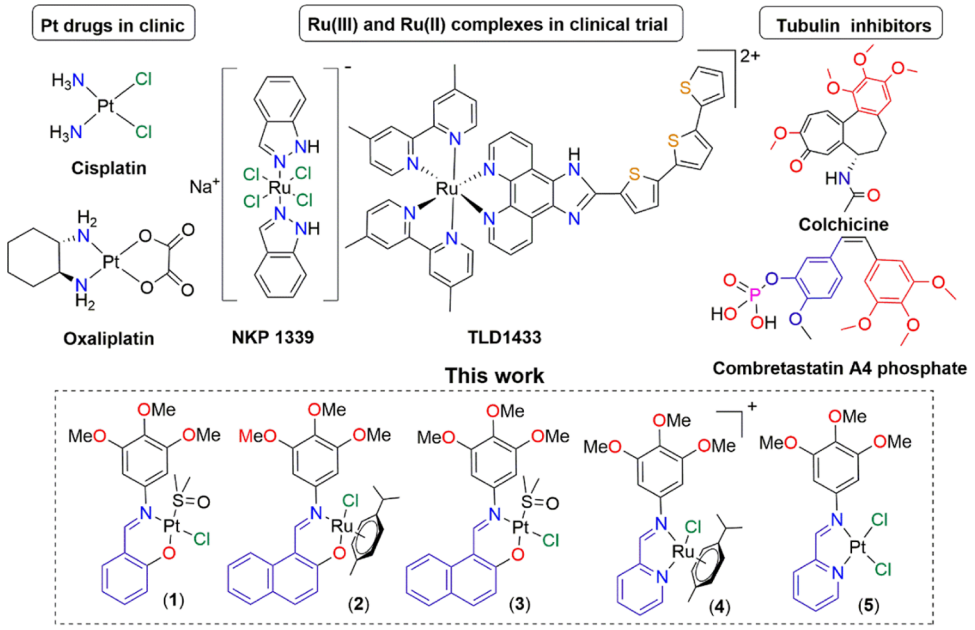

Figure 1. Top row: Two FDA-approved clinical Pt(II) drugs cisplatin and oxaliplatin, Ru(III) complex NKP 1339, and Ru(II) complex TLD1433 in clinical trials. Two microtubule-disrupting agents colchicine and combretastatin A4 phosphate used in clinics. Bottom row: Ru(II) and Pt(II) complexes (**1**−**5**) of trimethoxyphenyl (TMP)-based Schiff bases with different chelating moieties used in this work.

as a photodynamic therapy (PDT) agent against BCG refractory high-risk nonmuscle invasive bladder cancer.[17] There are several organometallic half-sandwich Ru(II) complexes, *viz.*, RM175, RAPTA-C, and DW-1/2, which have shown promising activity in preclinical trials.[11,18−22] The advantages of these classes of complexes are the structural flexibility and the change of mode of action by changing the attached ligand(s), arene, and halides.[23−28] These classes of complexes are capable of targeting DNA as well as proteins and show promising activity against platinum-resistant cancer.

The organic ligand bound to the metal, i.e., organic directing molecule (ODM), may provide an advantage to tune the target specificity of these metal complexes. There are reports where different ODMs have been used as ligands with Pt(II)- and Ru(II)-based complexes to target different enzymes,[29,30] organelles,[31,32] receptors,[33−35] proteins,[36,37] as well as cancer stem cells.[38,39] Earlier, we have reported Ru(II) complexes of trimethoxyphenyl (TMP)-based Schiff bases disrupting the microtubule assembly.[40] Microtubules remain in a dynamic equilibrium, together with actin and intermediate filaments, to form the cytoskeleton of a cell. The extensive cross talk between actin and microtubules is particularly important for regulating cell shape and polarity during cell migration and division and maintaining the epithelial cell shape and function.[41] In the mitosis process, microtubules play a very important role by forming a mitotic spindle to separate the duplicated chromosomes before cell division. These features make them an important target for chemotherapeutic agents. In the past decade, many Pt(II/IV)- and Ru(II)-based complexes with different ODMs have been developed, which disrupt microtubule dynamics and display promising cytotoxic efficacy.[42−47] There are various microtubule-targeting agents (MTAs), *viz.*, vinca alkaloids, paclitaxel, colchicine, combretastatin-A4 phosphate, and plocabulin, that interfere with microtubule dynamics and inhibit tube formation, cell migration, and cell proliferation, leading to a significant change in the endothelial cell morphology, which causes a rapid vascular collapse. Therefore, most MTAs show promising antiangiogenic activity.[48−50] The phosphorylation of the receptor tyrosine kinase vascular endothelial growth factor 2 (VEGFR2) is an important step to promote angiogenic responses.[51] The activity of VEGFR2 depends on its dimerization, which needs a healthy cytoskeleton apart from other factors. For example, nocodazole, which inhibits actin polymerization, interferes with the VEGFR2 signaling by decreasing VEGF-A-dependent downstream phosphorylation of the ERK1/2 signaling pathway.[52] Thus, cytoskeleton-targeting agents act as inhibitors for VEGFR2 activity, affecting the angiogenic process.

In this work, we present a comparative study of five *N*,*N*- and *N*,*O*-coordinated Pt(II)−DMSO and Ru(II)−*p*-cymene complexes of TMA-based Schiff bases, exploring the differences in their stability, lipophilicity, cytotoxicity, disruption of microtubules, and VEGFR2 phosphorylation inhibition.

EXPERIMENTAL SECTION

All chemicals and solvents were purchased from multiple commercial sources and used as received unless otherwise specified. Dichloromethane (DCM) and methanol were dried using standard procedures prior to use. $RuCl_3{\cdot}xH_2O$ was purchased from Precious Metals Online. The metal precursor complexes $[Pt(DMSO)_2Cl_2]$ and $[Ru_2^{II}(\eta^6\text{-}p\text{-cym})_2(Cl)_4]$ were synthesized as per the standard literature procedures.[53,54] 9-Ethylguanine (9-EtG) was purchased from Sigma-Aldrich and used for binding experiments. The ultrapure water used was purified by a Milli-Q UV purification system (Sartorius Stedim Biotech SA). MTT [(3-(4,5-dimethylthiazol-2-yl)-2,5-diphenyltetrazolium bromide)] (USB) and different kinds of supplements and assay kits were purchased from Gibco and used as received. Antitubulin antibodies and the rhodamine phalloidin reagent were purchased from Abcam. All of the solvents used for spectroscopic measurements were of spectroscopy grade. For NMR spectra, a 99.8% deuterated solvent was purchased from Cambridge Isotope Laboratories, Inc. The ^{1}H NMR, ^{13}C NMR, and HMQC spectra were recorded using a 500 MHz Bruker Avance III spectrometer at room temperature (24−27 °C). The chemical shifts of the relevant compounds are reported in parts per million (ppm).

https://dx.doi.org/10.1021/acs.inorgchem.0c03820
Inorg. Chem. 2021, 60, 3418−3430

UV−visible measurements were performed using an Agilent Technologies Cary 300 Bio or Perkin-Elmer LAMBDA 35 spectrophotometer. Fourier transform infrared (FT-IR) spectra were recorded using a Perkin-Elmer SPECTRUM RX I spectrometer. All of the mass spectra (electrospray ionization mass spectrometry (ESI-MS)) were recorded in positive mode electrospray ionization using a Bruker maXis II instrument. Elemental analyses were performed with a Perkin-Elmer 2400 series II CHNS/O analyzer. Isolated yields of ^{1}H NMR pure compounds are reported.

Syntheses. *Synthesis of (E)-2-(((3,4,5-Trimethoxyphenyl)imino)-methyl)phenol (**HL1**).* **HL1** was synthesized using our previously reported procedure.[40]

*Synthesis of (E)-1-(((3,4,5-Trimethoxyphenyl)imino)methyl)-naphthalen-2-ol (**HL2**).* **HL2** was synthesized using the same procedure of **HL1** with minor modifications. Precisely to the solution of 3,4,5-trimethoxy aniline (1 mmol) in methanol (20 mL), 2-hydroxy-1-napthaldehyde (1 mmol) was added and stirred at room temperature for 8 h. The solution was then concentrated, leading to the formation of a yellow precipitate of the ligand, which was collected and dried in vacuum. Yield: 78%. ^{1}H NMR (DMSO-d_6, 500 MHz, 298 K): δ (ppm) 15.82 (1H, d, J = 5.0 Hz, −OH), 9.61 (1H, s, −CH═N), 8.50 (1H, d, J = 8.5 Hz) 7.92 (1H, d, J = 9.0 Hz), 7.80 (1H, d, J = 7.5 Hz), 7.56 (1H, m), 7.35 (1H, t, J = 7.5 Hz), 7.01 (1H, d, J = 9.0 Hz), 6.95 (2H, s), 3.89 (6H, s), 3.69 (3H, s) (Figure S1). ^{13}C NMR (DMSO-d_6, 125 MHz, 298 K): δ (ppm) 169.8, 155.3, 153.5, 139.9, 136.5, 136.2, 133.0, 128.9, 127.9, 126.6, 123.3, 122.0, 120.4, 108.4, 98.3, 60.1, 56.1 (Figure S2).

*Synthesis of [Pt^{II}(L1)(DMSO)Cl] (**1**).* The ligand **HL1** (0.1 mmol) was dissolved in dry methanol followed by addition of sodium acetate (0.1 mmol) and stirred at room temperature for 15 min under a nitrogen atmosphere. [Pt(DMSO)$_2$Cl$_2$] (0.1 mmol) was then suspended in 10 mL of dry methanol and added dropwise to the solution and stirred at room temperature for 24 h under inert conditions in the dark. A clear yellow solution was formed; this solution was then concentrated, and a few drops of diethyl ether were added, leading to a yellow precipitate of the desired product. The product was isolated, washed twice with Et$_2$O, and finally dried in vacuum. Yield: 65%. ^{1}H NMR (DMSO-d_6, 500 MHz, 298 K): δ (ppm) 8.36 (1H, s), 7.58 (1H, d, J = 8.0 Hz), 7.43 (1H, t, J = 7.7 Hz), 7.02 (2H, s), 6.88 (1H, d, J = 8.5 Hz), 6.72 (1H, t, J = 7.5 Hz), 3.86 (6H, s, −OMe), 3.66 (3H, s, −OMe), 2.53 (6H, s, -DMSO) (Figure S3). ^{13}C NMR (DMSO-d_6, 125 MHz, 298 K): δ (ppm) 163.6, 162.5, 152.3, 148.6, 136.9, 136.1, 134.6, 120.6, 119.3, 116.7, 102.7, 60.2, 56.1 (Figure S4). UV−vis [MeOH, λ_{max}, nm (ε/M^{-1}·cm^{-1})]: 299 (9200), 408 (4300); FT-IR (cm^{-1}): 1563 (s), 1473 (m), 1417 (s), 1285 (m), 1212 (s), 1130 (s), 1100 (s), 1004 (s), 981 (s), 740 (s). ESI-HRMS (Methanol) m/z (exp.): 617.0457 (617.0447). Anal. calcd for $C_{18}H_{22}ClNO_5PtS$: C, 36.34; H, 3.73; N, 2.35. Found: C, 36.60; H, 3.68; N, 2.34.

*Synthesis of [Ru^{II}(L2)(p-cymene)Cl] (**2**).* The ligand **HL2** (0.1 mmol) was dissolved in dry degassed methanol (10 mL) followed by addition of KOH (0.1 mmol) and stirred at room temperature for 15 min. [Ru^{II}(*p*-cymene)Cl$_2$]$_2$ (0.1 mmol) was dissolved in methanol, added in the dark at room temperature under a N_2 atmosphere, and stirred at 50 °C under the same conditions for 12 h. The solution was evaporated to dryness, dissolved in DCM, and filtered (to remove the generated KCl). The filtrate was then evaporated to dryness, washed several times with diethyl ether, and finally dried in vacuum to obtain the desired product. Yield: 62%. ^{1}H NMR (DMSO-d_6, 500 MHz, 298 K): δ (ppm) 8.57 (1H, s, −CH═N), 7.89 (1H, d, J = 8.5 Hz), 7.69 (1H, d, J = 9.0 Hz), 7.63 (1H, d, J = 8.6 Hz), 7.32 (1H, t, J = 7.7 Hz), 7.13 (1H, t, J = 7.2 Hz), 7.05 (2H, s), 6.98 (1H, d, J = 9.0 Hz), 5.48 (1H, d, J = 6.5 Hz, *p*-cym-H), 5.37 (1H, d, J = 6.0 Hz, *p*-cym-H), 5.31 (1H, d, J = 6.0 Hz, *p*-cym-H), 4.49 (1H, d, J = 5.5 Hz, *p*-cym-H), 3.86 (6H, s, −OMe), 3.73 (3H, s, −OMe), 2.00 (3H, s, *p*-cym−CH$_3$) 1.12 (3H, d, J = 7.0 Hz, isopropyl-*p*-cym), 1.09 (3H, d, J = 7.0 Hz, isopropyl-*p*-cym) (Figure S5). ^{13}C NMR (DMSO-d_6, 125 MHz, 298 K): δ (ppm) 165.5, 157.3, 155.0, 152.2, 135.7, 135.0, 134.4, 128.5, 127.3, 125.6, 124.9, 121.5, 119.0, 107.7, 101.7, 100.3, 97.0, 85.7, 83.7, 83.2, 81.1, 60.2, 55.9, 29.9, 22.2, 21.2, 18.0 (Figure S6). UV−vis [MeOH, λ_{max}, nm (ε/M^{-1}·cm^{-1})]:253(36566), 323 (13700), 434 (4600). FT-IR (cm^{-1}): 1562 (s), 1513 (s), 1479 (s), 1407 (s), 1346 (s), 1209 (m), 1106 (s), 990 (m). ESI-HRMS (Methanol) m/z (exp.): 572.1361 (572.1369). Anal. calcd for $C_{30}H_{32}ClNO_4Ru$: C, 59.35; H, 5.31; N, 2.31. Found: C, 59.84; H, 5.35; N, 2.36.

*Synthesis of [Pt^{II}(DMSO)(L2)Cl] (**3**).* Complex **3** was synthesized by following the exact same procedure of **3** using [Pt^{II}(DMSO)$_2$Cl$_2$] as a precursor, which resulted in a yellow complex. Yield: 74%. ^{1}H NMR ($CDCl_3$, 500 MHz, 298 K): δ (ppm) 8.42 (1H, s), 7.81 (1H, d, J = 9.5 Hz), 7.71 (2H, t, J = 8.7 Hz), 7.52 (1H, t, J = 7.7 Hz), 7.33−7.29 (3H, m), 6.93 (2H, s), 3.96 (6H, s, −OMe), 3.87 (3H, s, −OMe), 3.32 (6H, s, -DMSO) (Figure S7). ^{1}H NMR (DMSO-d$_6$, 500 MHz, 298 K): δ (ppm) 8.60 (1H, s), 8.13 (1H, d, J = 8.5 Hz), 7.95 (1H, d, J = 9.5 Hz), 7.82 (1H, d, J = 7.5 Hz), 7.56 (1H, t, J = 7.7 Hz), 7.34 (1H, t, J = 7.2 Hz), 7.21 (1H, s), 7.10 (1H, d, J = 9.0 Hz), 3.91 (6H, s, −OMe), 3.68 (3H, s, −OMe), 2.53 (6H, s, -DMSO) (Figure S8). ^{13}C NMR ($CDCl_3$, 125 MHz, 298 K): δ (ppm) 164.7, 156.7, 153.1, 149.5, 137.9, 137.3, 133.2, 129.2, 128.2, 127.7, 123.8, 122.9, 120.0, 112.2, 102.8, 61.3, 56.7, 46.2 (Figure S9). UV−vis [MeOH, λ_{max}, nm (ε/M^{-1}·cm^{-1})]: 244 (43 000), 330 (11 600), 429 (6900); FT-IR (cm^{-1}): 1577 (m), 1555 (m), 1515 (s), 1478 (s), 1213 (s), 1131 (s), 1102 (s), 1002 (s), 988 (s). ESI-HRMS (Methanol) m/z (calc.): 609.1047 (609.1018). Anal. calcd for $C_{22}H_{24}ClNO_5PtS$: C, 40.97; H, 3.75; N, 2.17. Found: C, 40.54; H, 3.72; N, 2.16.

*Synthesis of [Ru(p-cym)(L3)Cl]PF$_6$ (**4**).* Briefly, 1.1 equiv of pyridine-2-aldehyde and 1 equiv of 3,4,5-trimethoxy aniline were dissolved in dichloromethane (DCM) at room temperature. The reaction was continued for 24 h in the dark. The solvent was then evaporated, and the sticky mass was washed with petroleum ether twice to remove excess aldehyde. The solid was then dissolved in diethyl ether and filtered to get rid of unreacted amine. The filtrate was dried to obtain a dark-orange solid (**L3**). The weighing of the solid suggested that the yield was 66%. However, as the ligand has a tendency to dissociate in reactants, it was reacted quickly. The ligand (0.2 mmol) was dissolved in dichloromethane and added to a dichloromethane solution of [Ru$_2^{II}$(η^6-*p*-cym)$_2$Cl$_4$] (0.1 mmol), followed by stirring for 8 h in the dark. An orange-red solution was obtained. The reaction mixture was evaporated and redissolved in methanol containing 1 equiv of NH_4PF_6. Then, the mixture was stirred for another 30 min at room temperature. An orange-red solid mass was obtained after evaporation of the mixture. The solid mass was dissolved in dichloromethane and filtered. The filtrate was evaporated and washed twice with diethyl ether to remove excess ligand and to obtain the pure product. Yield: 76%. ^{1}H NMR (DMSO-d_6, 500 MHz, 298 K): δ (ppm) 9.54 (1H, d, J = 5.5 Hz), 8.85 (1H, s), 8.30 (1H, t, J = 7.7 Hz), 8.24 (1H, d, J = 7.5 Hz), 7.87 (1H, m), 7.16 (2H, s), 6.04 (1H, d, J = 6.5 Hz, *p*-cym-H), 5.78−5.73 (2H, m, *p*-cym-H), 5.58 (1H, d, J = 6.0 Hz, *p*-cym-H), 3.88 (6H, s, −OMe), 3.77 (3H, s, −OMe), 2.53 (1H, m), 2.16 (3H, s, *p*-cym−CH$_3$), 1.01 (6H, d, J = 7.0 Hz) (Figure S10). ^{13}C NMR (DMSO-d_6, 125 MHz, 298 K): δ (ppm) 167.2, 156.0, 154.4, 152.9, 147.8, 140.0, 138.3, 129.9, 128.9, 105.5, 103.1, 100.3, 86.5, 85.8, 85.6, 85.4, 60.4, 56.3, 30.6, 21.7, 21.6, 18.3 (Figure S11). UV−vis.: [MeOH, λ_{max}, nm (ε/dm^3 mol^{-1} cm^{-1})]: 269 (12800), 369 (7100). FT-IR (cm^{-1}): 1576 (w), 1484 (m), 1446 (m), 1219 (m), 1108 (s), 983 (m), 822 (s). ESI-HRMS (Methanol) m/z (exp.): 543.1014 (543.0983) [$C_{25}H_{30}N_2O_3ClRu^+$], Anal. calcd for $C_{25}H_{30}N_2O_3ClRuPF_6$: C, 43.64; H, 4.40; N, 4.07. Found: C, 43.97; H, 4.38; N, 4.05.

*Synthesis of [Pt^{II}(L3)Cl$_2$] (**5**).* **L3** was isolated as described above, and 0.1 mmol of the ligand was dissolved in DCM. Pt(DMSO)$_2$Cl$_2$ (0.1 mmol) solution in DCM (10 mL) was added dropwise to the above solution and stirred at room temperature for 24 h in the dark. A yellow precipitate was obtained, which was isolated and washed twice with (3:1 v/v) diethyl ether and a DCM mixture, followed by washing with diethyl ether. Yield: 65%. ^{1}H NMR (DMSO-d_6, 500 MHz, 298 K): δ (ppm) 9.49 (1H, d, J = 6.0 Hz), 9.32 (1H, s), 8.44 (1H, m), 8.22 (1H, d, J = 8.0 Hz), 7.98 (1H, m), 6.91 (2H, s), 3.82 (6H, s, −OMe), 3.71 (3H, s, −OMe) (Figure S12). ^{13}C NMR (DMSO-d_6, 125 MHz, 298 K): δ (ppm) 171.8, 157.0, 151.9, 148.9, 142.5, 140.6, 137.6, 129.5, 129.4, 102.6, 60.1, 56.0 (Figure S13). UV−vis.: [DMF,

https://dx.doi.org/10.1021/acs.inorgchem.0c03820
Inorg. Chem. 2021, 60, 3418−3430

λ_{max}, nm (ε/dm^3 mol^{-1} cm^{-1})]: 270 (13 800), 408 (6000). FT-IR (cm^{-1}): 1578 (m), 1484 (s), 1448 (m), 1405 (m), 1218 (s), 1109 (s), 994 (s). ESI-HRMS (Acetonitrile) m/z (calc.): 560.0078 (560.0089) [$C_{25}H_{30}N_2O_3ClRu^+$], Anal. calcd for $C_{15}H_{16}Cl_2N_2O_3Pt$: C, 33.47; H, 3.00; N, 5.20. Found: C, 33.42; H, 2.99; N, 5.18.

Solution Stability and Binding Study. The hydrolytic stability of the complexes was studied using ESI-MS and ^{1}H NMR spectra (for **1** and **2**). The samples for ^{1}H NMR were prepared in 80% phosphate buffer in D_2O (20 mM, pD 7.4, containing 4 mM NaCl) and DMF-d_7 or DMSO-d_6. The complexes were first solubilized in organic solvents (DMF-d_7 for Pt or DMSO-d_6 for Ru complexes); then, the stock solutions were slowly mixed with phosphate buffer (20 mM, pD 7.4, containing 4 mM NaCl) such that the organic solvent and buffer ratio was 1:4 (v/v). For ESI-MS, the stock solutions of the samples were prepared in MeOH and then mixed to generate solutions with 1:9 v/v MeOH and 5 mM phosphate buffer having 4 mM NaCl at pH 7.4 and at 37 °C. The data were recorded after several time intervals. The binding abilities of the complexes (**1** and **2**) toward the model nucleobase 9-ethylguanine (9-EtG) were studied by incubating the samples with 2 equiv of 9-EtG, and the progress of the reaction was monitored using ESI-MS and ^{1}H NMR technique under the same aforementioned experimental conditions.

Distribution Coefficient Determination. Distribution coefficients of the five complexes were determined using the standard shake-flask method in an octanol−water system. NaCl (130 mM) was added into the aqueous layer to minimize the aqueous hydrolysis of the complexes. Each set of data was performed in duplicate, and the absorbance was recorded using a Carry 300 UV−vis spectrometer. Complexes were incubated for 4 h at 37 °C in a BOD incubator, and the concentration of the complexes present in octanol and water was determined. Distribution coefficient values ($\log D_{o/w}$) were obtained from the ratio of the complex's concentration in octanol and water.

Docking Studies. Molecular modeling was performed using GOLD (Genetic Optimization for Ligand Docking) Suite (Version 5.4.1) software from CCDC. GOLD adopts the genetic algorithm to dock molecules into protein (macromolecule) active sites, and a high GOLD score is an effective way of searching for more effective complexes. The GOLD score fitness value along with the inspection of the provided binding interaction provides better insight into the possible modes of binding. A colchicine derivative-bound tubulin protein (PDB ID: 1SA0) was used to dock the complexes. The complexes to be docked were first optimized using Gaussian 09 software by density functional theory (DFT) level of theory with B3LYP function and 6−31G(d,p) basis set for C, H, N, O, Cl, and LanL2DZ basis set for Ru(II) and Pt(II) centers. The conductor-like polarizable continuum model (CPCM) was used with water as the solvent during the optimization. Both the intact and the hydrolyzed complexes were chosen in the case of Pt(II) complexes, whereas for Ru complexes, only the hydrolyzed species were chosen for optimization because of the instant hydrolysis under physiological conditions. For receptor preparation, the PDB code 1SA0 was first downloaded from the Protein Data Bank. Then, an inhibitor-bound protein was optimized and its energy minimized by applying the OPLS 2005 force field by the protein preparation utility in Maestro Suite 2016−1 in Maestro (Schrödinger Suite 2016−1 Protein Preparation Wizard; Epik, Schrödinger, LLC, New York, NY, 2016; Impact, Schrödinger, LLC, New York, NY, 2016; Prime, Schrödinger, LLC, New York, NY, 2016) after removal of the water molecules. This optimized protein was used in GOLD Suite software, and the bound inhibitor was extracted. The optimized protein structure was used in the GOLD Docking wizard to add necessary hydrogen atoms. The colchicine derivative attached in the PDB of 1SA0 and extracted from the active site of the optimized protein was redocked into the protein to validate the docking study. The active site of the protein was defined as the colchicine-derivative binding site including 4 Å from its periphery. The binding sphere was large enough to cover the entire active site of the α and β tubulin interface. The GOLD software was run in the most accurate mode using the 200% accuracy option to generate the GOLD score and rescore the data with Chem Score.

Cell Lines and Culture Conditions. The following human cancer cell lines, *viz.*, pancreatic ductal carcinoma (MIA PaCa-2), hepatocellular carcinoma (Hep G2), and triple-negative human metastatic breast adenocarcinoma (MDA-MB-231), and the non-cancerous cell lines, *viz.*, human embryonic kidney (HEK-293) and human foreskin fibroblast (HFF-1), were obtained from NCCS, Pune, India. The cells were grown in 100 mm sterile tissue culture Petri dish flasks as an adherent monolayer in a 5% carbon dioxide atmosphere using a different culture media, supplemented with 10% fetal bovine serum (GIBCO) and antibiotics (100 units mL^{-1} penicillin and 100 μg mL^{-1} streptomycin). MIA PaCa-2 and HEK-293 were cultured in Dulbecco's modified Eagle's medium (DMEM), Hep G2 and HFF-1 were grown in minimal essential medium (MEM), and MDA-MB-231 was cultured in Dulbecco's modified Eagle's medium (DMEM) in a 1:1 mixture of DMEM with Ham's F12 nutrient mixture (*i.e.*, DMEM/F12), respectively. All cell lines were maintained at their logarithmic phase of growth before each experiment and plated when it reached 70% confluency.

Cell Viability Assay. The effect of the complexes toward different cancer (MDA-MB-231, MIA PaCa-2, and Hep G2) and noncancerous cell lines (HEK-293 and HFF-1) was evaluated using MTT assay. In brief, 6×10^3 (for slow-growing HFF-1, 1×10^4) cells per well were seeded in 96-well microplates with the respective media (200 μL) and incubated at 37 °C in a 5% carbon dioxide atmosphere. After 24 h of incubation, the compounds to be studied were added at appropriate concentrations. The water-insoluble complexes were first dissolved in DMSO (for cisplatin and oxaliplatin, we used DMF),[55] and then the stock solution was prepared by adding an appropriate volume of media containing 10% fetal bovine serum (FBS). The desired range of concentrations was prepared from the main stock solution by further diluting with the cell culture media such that the total DMSO or DMF concentration in the wells did not exceed 0.2%. After incubation with the drugs for a 72 h period, the drug-containing medium was removed and 200 μL of fresh medium containing 1 mg mL^{-1} MTT was added and incubated further for 3−3.5 h. Then, the MTT-containing medium was removed, and the formazan crystals were dissolved in 200 μL of DMSO. The growth inhibition of the cells was analyzed by measuring the relative absorbance of the drug-treated wells with respect to the untreated ones at 570 nm using BIOTEK ELx800 and BIOTEK Synergy H1M plate readers. IC_{50} values of the drug concentration needed for 50% reduction of the survival, based on the survival curve, were calculated by fitting nonlinear curves of cell viability (%) vs log of the drug concentration in micromolar in GraphPad Prism 5 Ver 5.03, using a four-parameter variable slope model. Each concentration was performed in triplicate in the MTT assay.

Effect on Tubulin Polymerization. Briefly, 1×10^5 number of MDA-MB-231 cells were grown over glass coverslips (Corning Life Sciences) for 48 h. The cells were then treated with complexes **1**−**3** for 6 h with two different concentrations. After 6 h, the medium containing drugs was removed and washed twice with chilled 1× PBS. The cells were then fixed with 4% (v/v) paraformaldehyde and kept at room temperature for 20 min. Then, PFA was removed, and the cells were quenched with NH_4Cl (50 mM). Next, the cells were washed with 1× PBS three times, followed by blocking with 3% bovine serum albumin (BSA, w/v) in PBS containing 0.1% Tween 20 (PBST) for 1 h at room temperature. After removing the BSA, the cells were incubated with a primary antibody against α-tubulin (anti-α tubulin antibody, EP1332Y, rabbit monoclonal microtubulin marker) in 1:400 dilution for 2.5 h at room temperature, followed by washing with 1× PBST three times. The secondary antibody solution of goat antirabbit IgG H&L (Alexa Fluor 488) was prepared in 1:750 dilution, to which rhodamine phalloidin reagent with 1:1000 dilution was added. The cells were incubated with this mixture for 2.5 h in the dark at room temperature, followed by washing twice with PBST and PBS. the cells were then mounted on slides for imaging using the Fluoroshield mounting medium containing 4′,6-diamidino-2-phenylindole (DAPI). All images were obtained using a Leica SP8 confocal microscope at 63× resolution.

https://dx.doi.org/10.1021/acs.inorgchem.0c03820
Inorg. Chem. 2021, 60, 3418−3430

Scheme 1. Representative Synthetic Procedure of the Ligands (HL1, HL2, and L3) and Metal Complexes (1−5)

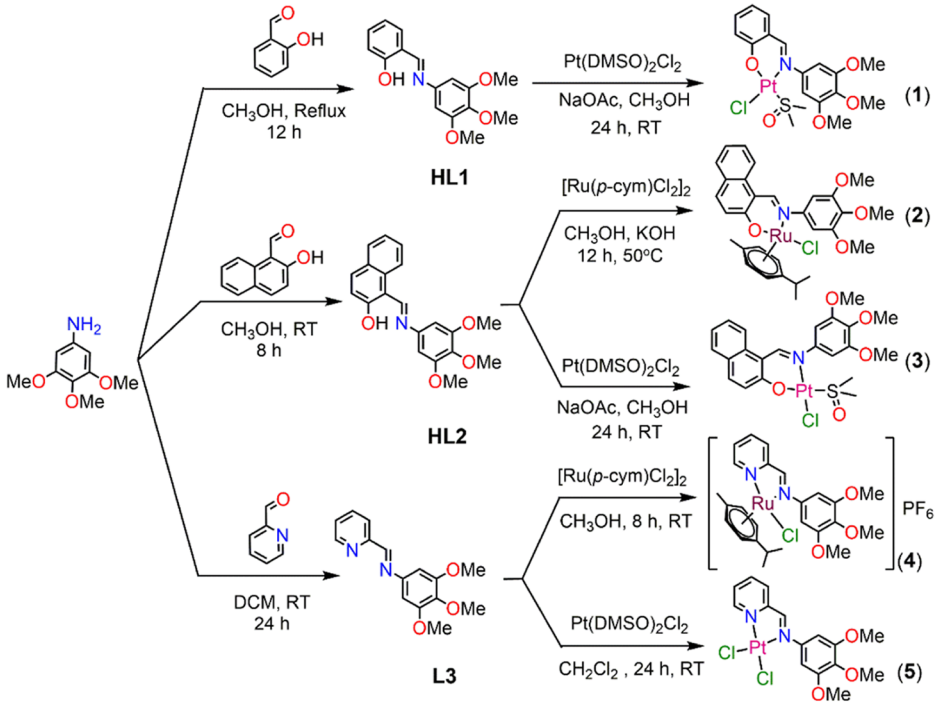

VEGFR2 Phosphorylation by Immunoblot. MDA-MB-231 cells were grown in DMEM/Ham's F12 (1:1 v/v) medium supplemented with 10% FBS and antibiotics at 37 °C in 5% CO_2. The abilities of **1** and **2** on VEGFR2 activation were tested by incubating the cells at 80% confluency with indicated concentrations of respective compounds for 6 h. DMSO (0.1%) was used as a control. VEGFR2 was activated by treating the cells with 60nM VEGF165a for 5 min. The activated cells were harvested and lysed by sonication in RIPA lysis buffer containing 25 mM Tris/HCl at pH 7.5, 1 mM ethylenediamine tetraacetic acid (EDTA), 100 mM NaCl, 1% Nonidet P40, 1% Triton-x 100 supplemented with 0.1 mM vanadate, and a protease-inhibitor cocktail (5 mg/L leupeptin, 0.1 mM phenylmethylsulphonyl fluoride, 2 mM benzamidine). The cell lysate was cleared by centrifuging at 15 000*g* for 10 min. The samples were boiled in Laemmli sample buffer and resolved by running through 6% sodium dodecyl sulfate polyacrylamide gel electrophoresis (SDS-PAGE). The protein was transferred onto nitrocellulose paper and blocked with 5% skimmed milk for 2 h at room temperature. The membrane was then incubated overnight at 4 °C with an anti-VEGFR2 antibody (catalog no. 2479S) or with an anti-1175 phosphotyrosine antibody (catalog no. 2478T) for 2 h. The amount of VEGFR2 and the level of phosphorylation were detected with a HRP-conjugated antirabbit secondary antibody. Normalized tyrosine phosphorylation was determined from the densitometric analysis of the respective blot, using the program ImageJ.

Cell Cycle Arrest. MDA-MB-231 cells (2×10^5 per plate) were grown in a 6-well plate suspended in 2 mL of DMEM medium for 48 h. Then, the medium was removed and complexes **1** and **2** with different concentrations were added, respectively. After 12 h of drug exposure, cells were harvested by treating with Accutase, centrifuged, and washed twice with cold 1× PBS buffer (pH 7.2). The cells were then suspended in 300 μL of cold 1× PBS buffer and fixed with 70% aqueous ethanol for 2 days at −20 °C. DNA staining was performed by resuspending the cell pellets in 1× PBS solution containing PI (55 μg mL^{-1}) and RNaseA (100 μg mL^{-1}) solutions. Cell suspensions were gently mixed and incubated at 37 °C for half an hour. Then, the samples were analyzed using a BD Biosciences FACS Calibur flow cytometer.

Detection of Apoptosis: Annexin V-PE Assay. Apoptotic cells were detected using a Annexin V-PE and 7-AAD dual staining apoptosis detection kit (BD Pharmingen) by flow cytometry according to the manufacturer's protocol. Briefly, 2×10^5 number of MDA-MB-21 cells were seeded in the 6-well plate suspended in 2 ml of DMEM medium. Then, the cells were incubated at 37 °C under a 5% carbon dioxide atmosphere for 48 h. Subsequently, the medium was removed, and the cells were treated with **1** and **2** with different concentrations for 12 h. The cells were then harvested by cold 1× PBS containing 0.1 mM EDTA, subsequently washed twice with cold 1× PBS, and finally resuspended in the supplied Annexin V binding buffer. Then, both Annexin V-PE and 7-AAD were added to the solution and incubated in the dark for 15 min at 25 °C. Data were analyzed using a BD Biosciences FACSVerse flow cytometer within 1 h of sample preparation.

RESULT AND DISCUSSION

Syntheses and Characterization. The *N,O*-coordinated ligands **HL1** and **HL2** were synthesized by reacting trimethoxy aniline with salicylaldehyde and 2-hydroxynapthaldehyde, respectively. The platinum derivatives (**1**, **3**) were obtained by addition of sodium acetate (NaOAc), followed by $[Pt(DMSO)_2Cl_2]$, to the methanolic solutions of **HL1** and **HL2**, respectively, as shown in Scheme 1. The ruthenium analogue (**2**) was prepared following the literature procedure, by reacting **HL2** in the presence of KOH with $[Ru(p\text{-cymene})_2Cl_2]_2$ in methanol at room temperature for 12 h (Scheme 1). The *N,N*-coordinated ligand **L3** was synthesized by stirring trimethoxy aniline and pyridine-2-aldehyde in DCM at room temperature. Immediately after isolation, complexation was carried out with the appropriate metal precursor $[Ru(p\text{-cymene})_2Cl_2]_2$ and $Pt(DMSO)_2Cl_2$ at room temperature in DCM for 8 and 24 h to obtain complexes **4** and **5**, respectively. All of the complexes herein reported are new and air-stable solids isolated in a moderate yield and well-characterized by ^1H NMR, ^{13}C NMR, ESI-HRMS, FT-IR spectroscopy, and UV−vis analysis. Bulk purities were confirmed by elemental analysis. The chemical shift of the imine proton of the free ligand (**HL2**) appears at 9.6 ppm as

https://dx.doi.org/10.1021/acs.inorgchem.0c03820
Inorg. Chem. 2021, 60, 3418−3430

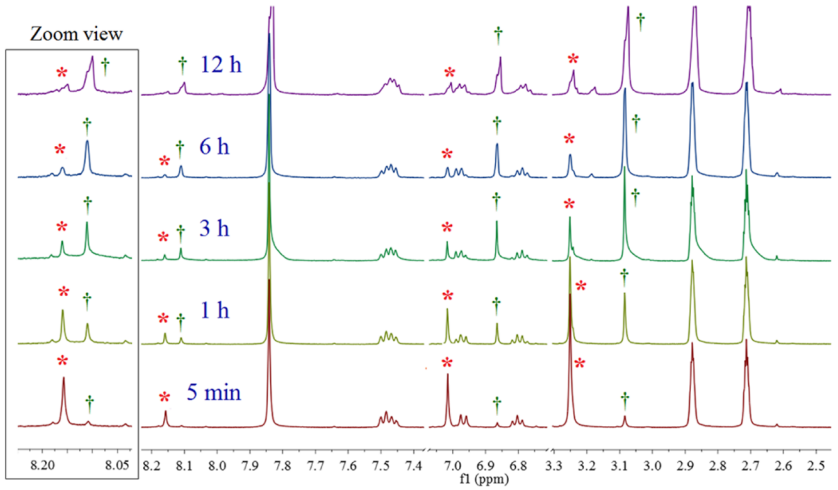

Figure 2. ^{1}H NMR spectra of **1** in 80% phosphate buffer in D_2O (20 mM, pD 7.4, containing 4 mM NaCl) and DMF-d_7 observed for 24 h. "*" indicates intact complex **1** and "†" represents the chloride-released aquated product of **1** having formulation $[Pt^{II}(L1)(DMSO)(H_2O)]^+$. The speciation is also supported by ESI-MS data presented in the Supporting Information.

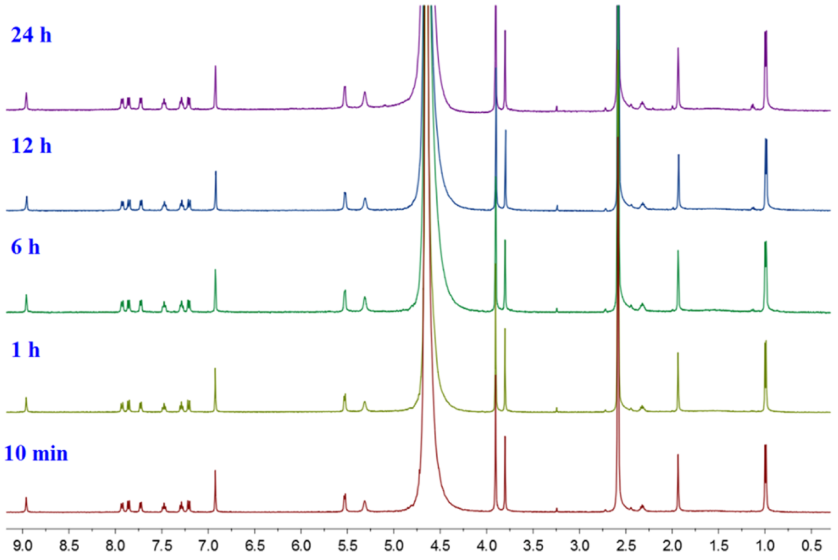

Figure 3. Solution stability of **2** in 80% phosphate buffer in D_2O (20 mM, pD 7.4, containing 4 mM NaCl) and DMSO-d_6 monitored by ^{1}H NMR.

per the ^{1}H NMR spectra. However, after metal complexation with Ru (**2**) and Pt (**3**), this imine proton shifts upfield to 8.5 and 8.6 ppm, respectively. In the case of Pt(II) complexes (**1** and **3**), the $-CH_3$ group of DMSO attached to the Pt center shifted to 2.54 ppm due to the electron-withdrawing nature of the Pt(II) center. The four aromatic protons of the *p*-cymene ring of Ru(II) complex **2** show a splitting pattern of 1 + 1 + 1 + 1 at 5.4−5.3 ppm, whereas **4** shows a splitting pattern of 1 + 2 + 1 at 6.0−5.5 ppm region in the ^{1}H NMR using DMSO-d_6. The stretching frequency corresponding to the imine (C═N) is in the range of 1560−1580 cm^{-1} in all of the complexes. In the case of Pt(II) complexes (**1** and **3**), a strong band appears at ca. 1004 cm^{-1}, which corresponds to the stretching frequency of S═O of the coordinated DMSO. The UV−vis spectra of these two complexes in methanol showed two bands at around 300−330 nm and 408−430 nm, which may be attributed to the $\pi-\pi^*$ and n$-\pi^*$ transition, respectively.[56,57] In Ru complex **2**, these two bands appear at around 323 and 434 nm. On the other hand, the corresponding UV−vis bands for **L3**-coordinating Ru(II) and Pt(II) complexes (**4** and **5**) appear at around 269−270 and 370−410 nm, respectively. All of the complexes are neutral, except *N*,*N*-coordinated Ru(II) derivative **4**, which is monocationic in nature. Therefore, in the ESI-MS positive mode, the *m*/*z* formulations of the Pt(II) complexes correspond to $[Pt(L1/L2)(DMSO)(Cl)]Na^+$ for **1** and **3** and $[Pt(L3)(Cl)_2]Na^+$ for **4**. However, for Ru(II) complexes, the formulations are $[Ru(L2)(p\text{-cym})]^+$ for **2** and $[Ru(L3)(p\text{-cym})Cl]^+$ for **5**.

Stability in Aqueous Solution. The stability of the complexes was studied in phosphate buffer solution (pH 7.4, containing 4 mM NaCl) using ESI-MS and/or ^{1}H NMR. In general, *N*,*O*-coordinated Ru(II) complexes undergo rapid aquation under physiological conditions, and we had previously reported that the ruthenium complex of **HL1** undergoes rapid aquation in buffer solution and the aquated complex remains stable for a period of at least 24 h.[40] The Pt(II) derivative **1** of the same ligand **HL1** was also probed for solution stability using both ^{1}H NMR and ESI-MS to understand whether the change of the metal center and the coordination mode affects the stability of the complexes. The

https://dx.doi.org/10.1021/acs.inorgchem.0c03820
Inorg. Chem. 2021, 60, 3418−3430

^{1}H NMR data (Figure 2) in 4:1 (v/v) phosphate buffer in D_2O (20 mM, pD 7.4, containing 4 mM NaCl) and DMF-d_7 showed that for **1** the aquation started immediately (by releasing the attached chloride) and the amount of the aquated adduct increased slowly over time, unlike the rapid aquation observed in the case of pseudo-octahedral Ru(II) complexes. It took 12 h for most of the complex to be converted to its monoaquated form (Figure 2). This observation was also confirmed from ESI-MS data in 9:1 (v/v) phosphate buffer (5 mM, pH 7.4, and containing 4 mM NaCl) and methanol, which showed that the relative intensity of the intact complex at m/z 617.0410 (calcd 617.0447) sharply decreased over time and the species at m/z 559.0877 (calcd 559.0861) and 577.0985 (calcd 557.0967) corresponding to the formulations of $[Pt(L1)(DMSO)]^+$ and $[Pt(L1)(DMSO)(OH_2)]^+$, respectively, mainly dominated in the solution. The hydrolyzed adduct remained stable up to 24 h, which is also supported by ESI-MS (Figures S15−S18). The coordination environment of Pt(II)-napthoxy derivative **3** is similar to that of **1**; therefore, the solution stability was monitored through ESI-MS. Complex **3** shows a hydrolysis pattern similar to that of **1** (Figures S19 and S20). Ru(II)-napthoxy derivative (**2**), on the other hand, upon dissolution in buffer solution (1:4 v/v DMSO-d_6 in phosphate buffer, pH 7.4) undergoes rapid chlorido hydrolysis by water and forms the monoaquated species immediately, which is also confirmed by addition of $AgNO_3$ to a solution of **2** providing the same ^{1}H NMR spectra. The immediate hydrolysis of neutral *N,O*-coordinated Ru(II) complexes is well supported by the literature, which suggests that the shift from a neutral *N* donor to an anionic *O* donor drastically increases the hydrolysis rate of the Ru(II)−*p*-cymene complexes.[58−60] The monoaquated species remain stable for 24 h, which is confirmed by both ^{1}H NMR and ESI-MS studies (Figures 3, S21, and S22). *N,N*-coordinated Ru(II) pyridine derivative (**4**) underwent slower hydrolysis, and the relative abundance of the hydrolyzed product increased over time and ultimately reached an equilibrium. Even after 24 h, a significant amount of intact **4** remained in the solution (Figures S23−S25). However, the poor solubility of Pt(II)-pyridine derivative (**5**) prevented us from conducting its solution studies in the aforementioned solution conditions. Therefore, from solution studies, it can be concluded that the neutral *N,O*-coordinated Ru(II) complexes undergo rapid aquation in the buffer solution (pH 7.4) and produce a stable aquated product, whereas for *N,O*-coordinated Pt(II)−DMSO complexes exhibit slow hydrolysis, and most of the complexes are converted into the monoaquated form only after 12 h. This difference in the hydrolysis pattern may be due to the higher covalency of the relevant bonds formed by Pt(II), causing the dissociation of the Pt−Cl bond to be slower. In addition, the presence of the π-donor *p*-cymene moiety in Ru(II) in an η^6 fashion further increases the electron density on the Ru(II) center in *N,O*-coordinated complex **2**, weakening the Ru−Cl bond and leading to its quick dissociation. Compared to the neutral complexes of the anionic *N,O* donor ligands, the monopositive complexes of the neutral *N,N* donor ligands make the Ru−Cl bond more inert, leading to better stability and slower hydrolysis.

Distribution Coefficient Determination. Lipophilicity refers to the ability of a compound to dissolve in fats, lipids, nonpolar solvents, as well as aqueous media. The cytotoxic efficacy of a compound is often correlated with lipophilicity. Lipophilicity is determined by the ratio of the compound concentration in an octanol−water system using the shake-flask method.[61] Hydrophobicity promotes hydrophobic interaction with protein targets[62] and the lipophilic cell membrane. Therefore, the potency of an organometallic complex increases with increase in hydrophobicity.[63,64] The octanol−water distribution coefficient values ($\log D_{o/w}$) of the *N,O*-coordinated complexes are ca. 1.5, 1.0, and 2.2 for **1**, **2**, and **3**, respectively (Figure 4). This indicates that the *N,O*-coordinated complexes are lipophilic in nature, and changing the metal to platinum and incorporating the 2-hydroxynapthyl group increases the hydrophobicity further. On the other hand, the log D value of the *N,N*-coordinated pyridine derivatives **4** is ca. −0.6, indicating that the monocationic Ru complex (**4**) is hydrophilic in nature. However, the $\log D_{o/w}$ value of the corresponding Pt(II) analogue (**5**) was not measured due to its poor solubility in octanol and aqueous mixtures.

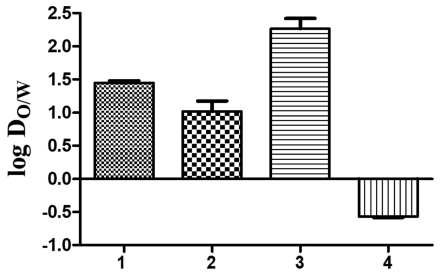

Figure 4. Distribution coefficient of the complexes (**1**−**4**) in 1:1 (v/v) octanol−water mixture at 37 °C.

***In Vitro* Cytotoxicity.** We observed that the stability and lipophilicity of the complexes were dependent on their coordination mode, the metal ion, and the geometry of the complexes. Therefore, to understand the effect of structural variation on cytotoxicity, *in vitro* IC_{50} values of all of the complexes (**1**−**5**) were assessed against three different cancer cells under normoxic conditions by MTT assay. The cell lines that were chosen to evaluate the toxicity profiles were triple-negative human metastatic breast adenocarcinoma MDA-MB-231, pancreatic ductal carcinoma MIA PaCa-2, and hepatocellular carcinoma Hep G2. All of the cancer cells chosen are aggressive, and, importantly, the triple-negative breast cancer (TNBC) MDA-MB-231 is a highly invasive and metastatic cancer without a safe and effective therapeutic drug. The cytotoxicities of the complexes were also evaluated against two noncancerous cell lines, *viz.*, human embryonic kidney HEK-293 and human foreskin fibroblast HFF-1. The IC_{50} values listed in Table 1 show that complex **1** displays a IC_{50} value of ca. 2−3 μM against all of the tested cell lines. Our earlier report of the Ru(II) complex of the same ligand showed five times lower efficacy with IC_{50} ranging from ca. 10 to 15 μM against the same panel of cell lines, and the IC_{50} value remained the same even for 72 h of incubation. Hence, changing Ru(II)−*p*-cymene to Pt(II)−DMSO enhanced the cytotoxicity of the complexes. The Ru-napthoxy derivative **2** shows a IC_{50} value of ca. 6−8 μM, suggesting that the introduction of the 2-hydroxynapthyl group enhanced the cytotoxicity by 2−3 times compared to that of the salicylaldehyde or o-vanillin. The enhancement of the dose-response was also observed for the 2-hydroxynapthyl motif bearing Pt complex **3**. Complex **3** displayed the highest cytotoxicity with the IC_{50} ranging from 1 to 1.5 μM against the three cancer cell lines. The *N,N*-coordinated Ru(II) complex **4**,

https://dx.doi.org/10.1021/acs.inorgchem.0c03820
Inorg. Chem. 2021, 60, 3418−3430

Table 1. *In Vitro* Cytotoxicity of Complexes 1−5 in Various Cancer and Normal Cell Lines under Normoxic Conditions

	IC_{50} ± SD (μM)[a]				
complexes	MIA PaCa-2	Hep G2	MDA-MB-231	HEK-293	HFF-1
1	2.6 ± 0.2	2.5 ± 0.3	2.2 ± 0.1	3.7 ± 0.2	3.8 ± 0.2
2	6.1 ± 0.3	7.5 ± 0.4	5.5 ± 0.4	8.7 ± 0.7	7.7 ± 0.9
3	1.2 ± 0.2	1.4 ± 0.2	1.1 ± 0.1	2.0 ± 0.2	1.8 ± 0.1
4	>100	>100	>100	>100	>100
5	20.2 ± 1.0	21.4 ± 1.8	19.4 ± 0.8	N.D.	N.D.
oxaliplatin	5.7 ± 0.2[b]	9.8 ± 0.3[b]	19.2 ± 1.2	2.1 ± 0.4	7.0 ± 0.6[b]

[a]The medium used for drug addition had less than or equal to 0.2% DMSO or DMF and the IC_{50} ± SD was determined by the MTT assay in normoxia (~15% O_2). IC_{50} values were calculated by a nonlinear four-parameter curve fitting in a dose-response inhibition−variable slope model using GraphPad prism. SD = standard deviation. Indicative plots are provided in the ESI, Figures S26 and S27. The data presented are mean of at least three independent experiments; in a single experiment, each concentration was assayed in triplicate. The statistical significance (P) of the data is >0.001 to <0.05. [b]Oxaliplatin; data have been taken from our previous report.[65] N.D. stands for not determined.

in spite of having higher kinetic stability under physiological conditions, was not toxic even up to 100 μM, but the corresponding platinum analogue showed moderate cytotoxicity (IC_{50} ca. 18−22 μM). There are reports of new Ru(II) and Pt(II) complexes showing selectivity toward cancer cells;[26,65,66] therefore, to evaluate a possible degree of selectivity against cancer cells, we have further tested the cytotoxicity of the complexes against fast-growing noncancerous kidney cell HEK-293 and normal foreskin fibroblast cell HFF-1. IC_{50} data suggest that the complexes are marginally less toxic to the fast-growing noncancerous cells HEK-293 and normal HFF-1 (Table 1). The *in vitro* toxicity profile of the complexes correlates well with the lipophilicity of the complexes. The *N*,*O*-bearing platinum complexes are more lipophilic than the ruthenium analogues. Moreover, introduction of the 2-hydroxynapthyl group in **3** further enhances the hydrophobicity, and hence **3** is most cytotoxic in the series, followed by **1** and **2**. In fact, our earlier reported Ru(II) complex of similar ligands[40] with lower lipophilicity showed a poor IC_{50} dose profile compared to **2**. The *N*,*N*-coordinated Ru complex **4** (with neutral **L3** ligand) is monocationic and most hydrophilic among the five complexes. Thus, traversing the cell membrane through passive diffusion may be difficult for **4**, rendering poor cytotoxicity. Therefore, the newly synthesized *N*,*O*-coordinated TMP-based Ru(II) and Pt(II) derivatives show promising cytotoxicity against the panel of various cell lines. The Pt(II) complexes **1** and **3** are most potent among the series and more toxic than the clinical Pt drugs cisplatin (IC_{50}: 14 ± 1 μM) and oxaliplatin (IC_{50}: 19.2 ± 1.2 μM) against MDA-MB-231 cells.

Effect on the Cellular Cytoskeleton of MDA-MB-231 Cells. We have previously found that the Ru complex of ligand **HL1** can disrupt the microtubule network in a dose-dependent manner. In this work, it has been observed that incorporating the 2-hydroxynapthyl group and replacing Ru(II)−*p*-cymene with Pt-DMSO enhances the cytotoxicity. Therefore, we first evaluated the microtubule disruption efficiency of the complexes by a docking study with a tubulin protein (PDB Id: 1SA0) using GOLD Suite software. The binding affinities of the complexes were determined by evaluating the GOLD score values and comparing them with the extracted inhibitor. The GOLD score and an inspection of the binding interactions support that the higher score represents better binding affinity. Since the Pt(II) complexes hydrolyze slowly in the solution, both the intact and the aquated species have been used for the docking experiment. On the other hand, due to the rapid hydrolysis of Ru analogue (**2**) in the solution, only the aquated species has been chosen for this study. Docking data suggest that both Pt and Ru complexes bind to the active site of the α−β tubulin assembly with distinct differences in their binding interactions where the Pt complexes bind at a closer vicinity of the inhibitor binding site compared to the Ru complexes (Figure S28). The docking results show that the interaction of the intact or monoaquated Pt complexes **1** and **3** is higher than that of the monoaquated Ru derivative (**2**) (Table S1). This supports the higher efficacy of the Pt(II)−DMSO complexes (**1** and **3**) toward cytotoxicity compared to that of the Ru(II)−*p*-cymene analogues. Therefore, all of the three efficient complexes (**1**−**3**) were investigated for their possible effect on the microtubule network. It is well known that actin, microtubule, and intermediate filaments form the basic cellular cytoskeleton, and extensive cross talk between them is required to maintain the core biological process and structural integrity.[41] Hence, MDA-MB-231 cells were stained with an anti-α-tubulin antibody interacting with a secondary antibody tagged with Alexa Fluor 488 (green) to stain microtubules and with rhodamine phalloidin (red) to stain the F-actin filaments. DAPI (blue) was used to visualize the nucleus. In the control, normal filamentous microtubules and the F-actin structure were observed. (Figure 5) MDA-MB-231 cells when treated with both **1** and **3** at two different concentrations (3.5 and 5 μM for **1** and 2 and 3 μM for **3**) exhibited disruption of the filamentous microtubule network within 6 h of treatment in a dose-dependent manner (Figure 5). The ability to disrupt the microtubule assembly within this short incubation period indicates that microtubule dynamics may be one of the targets of these TMP-conjugated Pt(II) complexes. Ru(II) complex **2** also disrupts the microtubule assembly in a dose-dependent manner within 6 h of incubation. Besides, some fragmented actin filaments were also observed in this case (Figure S29). Thus, TMP-conjugated Ru and Pt analogues (**1**−**3**) induce a dose-dependent damage to the cytoskeleton of MDA-MB-231 cells. The ability of the agile cytoskeleton to orchestrate the change in cell shape is essential for angiogenesis. Actin and microtubules play a key role in maintaining the agility of the intracellular matrix. The signaling by receptor tyrosine kinases depends on the intracellular matrix function as a platform beneath the plasma membrane that supports the assembling of receptor clusters.[67−69] Microtubules are important for maintaining the steady-state distribution of VEGFR2 in the endogenous pool and the plasma membrane.[52,70] Thus, the *in vivo* and *in vitro* studies with microtubule-targeting drugs display promising antiangiogenic activity and VEGFR2 inhibition.[48−50] Therefore, to check if disruption of the

https://dx.doi.org/10.1021/acs.inorgchem.0c03820
Inorg. Chem. 2021, 60, 3418−3430

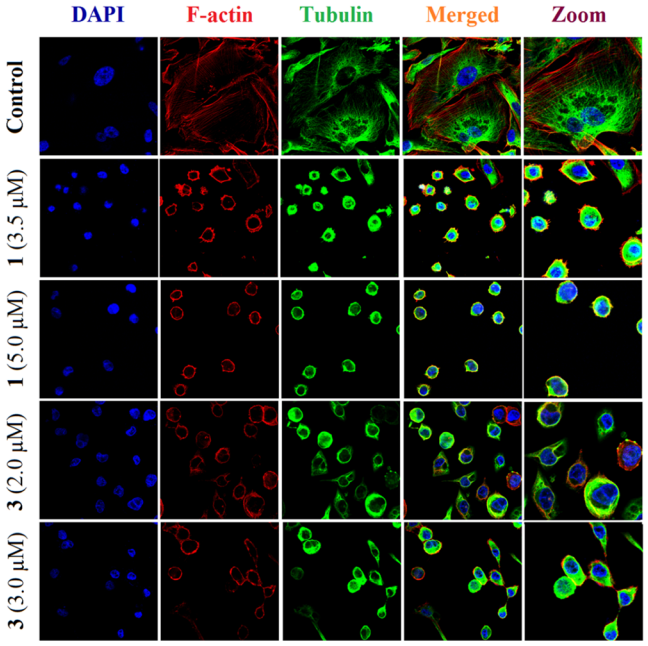

Figure 5. Immunofluorescence study of disruption of the microtubule network in MDA-MB-231 cells after incubation of 6 h in the presence of 0.1% DMSO and complexes **1** (3.5 and 5 μM) and **3** (2 and 3 μM). Microtubules were visualized with a monoclonal anti-α-tubulin antibody (green) interacting with a secondary antibody tagged with Alexa Fluor 488 (λ_{em} = 520 nm). F-actin (red) was stained with rhodamine phalloidin (λ_{em} = 647 nm). The blue color of the cell nucleus is due to staining with DAPI. Images were acquired using a Leica SP8 confocal microscope at 63× resolution.

microtubule network by **1** or **2** would inhibit VEGFR2 activation at the plasma membrane, we treated MDA-MB-231 cells with respective compounds and probed for autophosphorylation of tyrosine residues in its C-terminal tail (Figure 6). Following stimulation of VEGFR2 with its ligand VEGF-A ($VEGF_{165a}$), several tyrosine residues in the C-terminal tail were autophosphorylated. Here, we monitor the phosphorylation of an import tyrosine residue Y1175 in the C-terminal

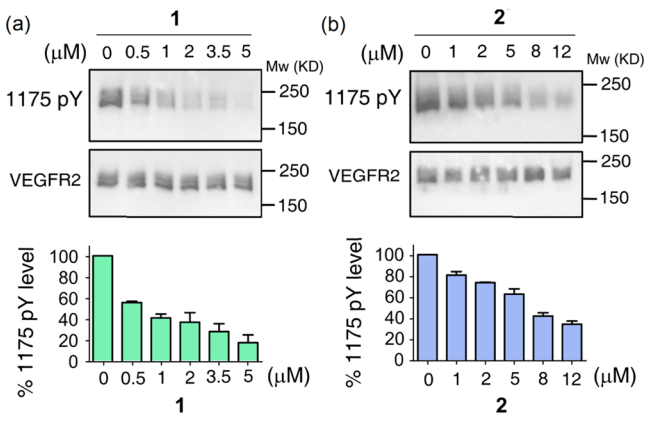

Figure 6. Effect of **1** and **2** on VEGFR2 activation. (a) and (b) are representative Western blot strips showing total VEGFR2 and Y1175 phosphorylation levels after treating the cells with **1** and **2** following activation with $VEGF_{165a}$. At the bottom of each panel, the bar plot represents the quantification of the Y1175 phosphorylation level at indicated concentrations of **1** and **2**. (n = two experiments; mean ± SD.).

tail that functions as an adaptor for downstream signaling.[71,72] We observed that none of the complexes affected the expression of VEGFR2 but rather reduced the autophosphorylation of Y1175 in a concentration-dependent manner upon 6 h of incubation. Thus, disruption of the microtubule network prevents ligand-dependent activation of VEGFR2 at the plasma membrane. This further shows that the complexes are capable of disrupting the microtubule network and, in turn, VEGFR2 activity, which leads to their efficacy against various forms of cancer.

Pathway of Cell Killing. We observed that all of the three *N,O*-coordinated TMP-conjugated metal complexes showed promising cytotoxicity and disrupted the microtubule assembly in a dose-dependent manner and also inhibited the VEGFR2 activity in MDA-MB-231 cells. However, the hydrolysis studies of the complexes suggest that the halides are labile under physiological conditions. Therefore, to check whether DNA is one of the targets of these Pt(II) and Ru(II) complexes, we performed the binding study of **1** and **2** with model nucleobase 9-ethylguanine (9-EtG) by ^{1}H NMR and/or ESI-MS. The ^{1}H NMR spectra of **1** in the presence of 2 equiv of 9-EtG in 20% DMF-d_7 in phosphate buffer (20 mM, pD 7.4, 4 mM NaCl) showed that it forms the mono-coordinated 9-EtG adduct within 1 h, which is confirmed by the shift of the H8 proton from 7.75 to 8.47 ppm (marked as H8*). In addition, within 3 h, a new peak corresponding to H8 started to appear significantly at 8.32 ppm (marked as H8**), which may be due to the formation of the bisadduct of 9-EtG (Figure 7A). This finding is also confirmed by ESI-MS where both the mono- and bisadducts of 9-EtG are observed at m/z 738.1682 (calcd 738.1668) and 839.2346 (calcd 839.2336), respectively, after 2 h of incubation. The bis-9-EtG adduct increases over time, and after 24 h, it is predominantly present in the solution (Figures 7B and S30−S32). In contrast, the Ru(II)−*p*-cymene complex **2** of the 2-hydroxynapthyl ligand shows a very small amount of 9-EtG adduct only after 24 h, corresponding to m/z 751.2208 (calcd 751.2176) (Figures S33 and S34). This indicates that unlike the platinum complex **1**, DNA may not be a major target for **2**, which is also supported by our earlier studies.[26,40] This difference in the binding ability toward an external nucleophile may be linked with the reactivity of the molecule associated with the structural difference of the complexes. The aquated Ru complex **2** coordinated with a *p*-cymene (a π-donor ligand) ligand may increase the electron density at the Ru(II) center[73] compared to the DMSO-coordinated Pt(II) complexes having no such π-donor ligand, leading to the higher reactivity of the Pt(II) complexes toward external nucleophiles (*viz.*, 9-EtG)[24] (Scheme 2). This could also be a reason for the higher cytotoxicity of the Pt derivatives **1** and **3**.

Microtubules play an important role during the mitosis process; therefore, the ability of the complexes to disrupt the microtubule dynamics may lead to cell cycle arrest in the mitosis (M) phase. When we treated MDA-MB-231 cells with both complexes **1** and **2** and measured the relative DNA content in each phase of the cell cycle by flow cytometry, we found that with an increase in drug concentration, the percentage of arrest in the G2/M phase increased (Figure 8A and Table S1). Complexes **1** and **2** were investigated for their ability to induce apoptosis in MDA-MB-231 cells by Annexin V-PE and 7-AAD dual staining. The flow cytometry data show that after treating the cells with increasing concentrations for 12 h, the percentage of apoptotic MDA-

https://dx.doi.org/10.1021/acs.inorgchem.0c03820
Inorg. Chem. 2021, 60, 3418−3430

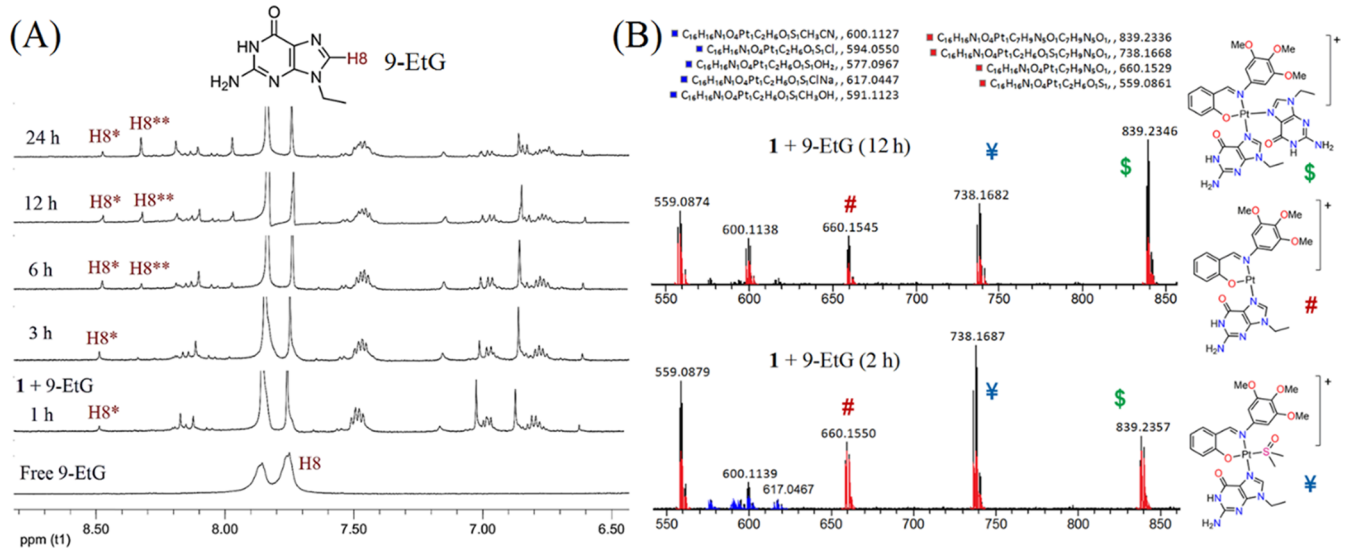

Figure 7. (A) ^{1}H NMR spectra of 9-ethylguanine (9-EtG) binding of **1** in 4:1 (v/v) phosphate buffer in D_2O (20 mM, pD 7.4, containing 4 mM NaCl) and DMF-d_7. H8* indicates a shift of the H8 proton due to formation of a monoadduct of 9-EtG and H8** represents the formation of a bis-9-EtG adduct. (B) ESI-MS spectra of the time-dependent 9-EtG binding of **1** in 9:1 (v/v) phosphate buffer (5 mM, pH 7.4, containing 4 mM NaCl) and methanol. The chemical structures of different 9-EtG adducts of **1** are shown separately.

Scheme 2. Proposed Mechanism of Hydrolysis, 9-EtG Binding, and Cell Killing of *N,O*-Coordinated Ru^{II} and Pt^{II} Complexes (1−3)

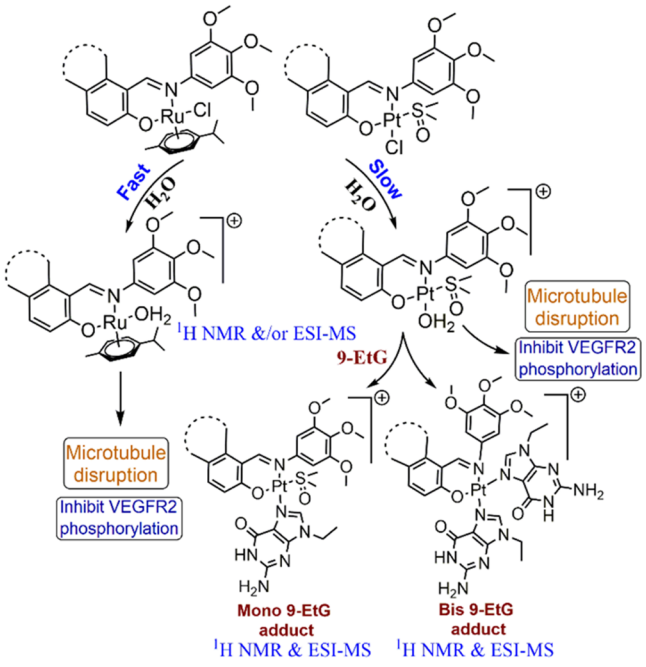

MB-231 cells increases (Figures 8B and S35), suggesting that the complexes kill the cells through the apoptotic pathway.

CONCLUSIONS

We have synthesized a series of *N,O*- and *N,N*-coordinated Pt(II) and Ru(II) complexes (**1**−**5**) with the trimethoxyphenyl group as a part of the ligand system. The *N,O* analogues (**1**−**3**) show excellent *in vitro* cytotoxicity against the tested cell lines, whereas changing the coordination to *N,N* drastically decreases the cytotoxic efficacy. The above is not a general trend and thus may be attributed to the ligands used. The stability studies suggest that the *N,O*-coordinated Ru(II) analogues hydrolyzed

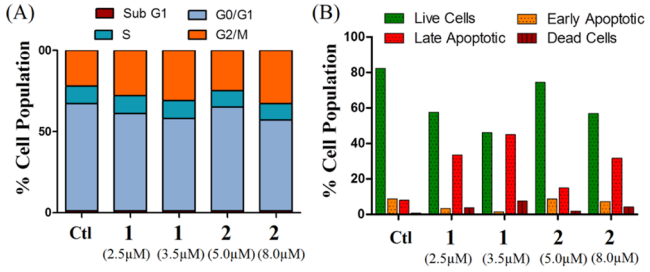

Figure 8. (A) Cell cycle arrest in the G2/M phase by **1** and **2** in a dose-dependent manner in the MDA-MB-231 cell line. (B) Induction of apoptosis by complexes **1** and **2** in the MDA-MB-231 cell line.

rapidly and that the monoaquated species remain stable under physiological conditions. However, the Pt(II) complexes display relatively slower aquation. Incorporation of the 2-hydroxynapthyl group increases the cytotoxicity of both the Pt(II) and Ru(II) complexes, albeit the enhancement is more pronounced in the square planar Pt(II)−DMSO complexes. Complex **3** with Pt(II) and the 2-hydroxynapthyl group is the most cytotoxic among the five complexes and ca. 5−10 times more toxic than clinical drugs oxaliplatin and cisplatin. All of the complexes (**1**−**3**) disrupt the microtubule assembly in a dose-dependent manner and arrest the cell cycle in the G2/M phase to induce apoptotic cell death. The complexes also inhibit VEGFR2 phosphorylation in a dose-dependent fashion. The Pt(II) complexes are not only more effective in microtubule disruption and inhibition of VEGFR phosphorylation but also have high affinity for 9-EtG in contrast to the Ru(II)−*p*-cymene complexes of the same bidentate ligands. Thus, DNA may be an additional target of the Pt(II) complexes, leading to their higher toxicity.

ASSOCIATED CONTENT

Supporting Information

The Supporting Information is available free of charge at https://pubs.acs.org/doi/10.1021/acs.inorgchem.0c03820.

https://dx.doi.org/10.1021/acs.inorgchem.0c03820
Inorg. Chem. 2021, 60, 3418−3430

NMR spectra of ligands (Figures S1 and S2) and complexes (Figures S3−S13); hydrolysis of the complexes in phosphate buffer (Figures S14−S25); *in vitro* cytotoxicity of the complexes by MTT assay (Figures S26 and S27); docking study (Figure S28 and Table S1); microtubule disruption; 9-EtG binding; and cell cycle analysis and apoptosis (Figures S29−S35 and Table S2) of the complexes (PDF)

AUTHOR INFORMATION

Corresponding Author

Arindam Mukherjee − *Department of Chemical Sciences and Centre for Advanced Functional Materials, Indian Institute of Science Education and Research Kolkata, Mohanpur 741246, India;* orcid.org/0000-0001-9545-8628; Email: a.mukherjee@iiserkol.ac.in

Authors

Sourav Acharya − *Department of Chemical Sciences and Centre for Advanced Functional Materials, Indian Institute of Science Education and Research Kolkata, Mohanpur 741246, India;* orcid.org/0000-0001-5511-1312

Moumita Maji − *Department of Chemical Sciences and Centre for Advanced Functional Materials, Indian Institute of Science Education and Research Kolkata, Mohanpur 741246, India;* orcid.org/0000-0003-3440-0881

Manas Pratim Chakraborty − *Department of Biological Sciences, Indian Institute of Science Education and Research Kolkata, Mohanpur 741246, India*

Indira Bhattacharya − *Department of Biological Sciences, Indian Institute of Science Education and Research Kolkata, Mohanpur 741246, India*

Rahul Das − *Department of Biological Sciences, Indian Institute of Science Education and Research Kolkata, Mohanpur 741246, India*

Arnab Gupta − *Department of Biological Sciences, Indian Institute of Science Education and Research Kolkata, Mohanpur 741246, India*

Complete contact information is available at: https://pubs.acs.org/10.1021/acs.inorgchem.0c03820

Author Contributions

The manuscript has been submitted with the consent of all authors. The outline of the work was planned by S.A. and A.M. Syntheses and characterizations were carried out by S.A., and *in vitro* cytotoxicity works were carried out jointly by S.A. and M.M. Hydrolysis and binding studies using ^{1}H NMR and ESI-MS were carried out by M.M. and S.A., respectively. Microscopy studies of tubulin were performed by I.B., and the results were verified by AG. The VEGFR2 assays were carried out by M.P.C., and the results were verified by R.D. *In vitro* mechanistic studies were performed jointly by S.A. and M.M. The whole work was performed under the supervision of A.G., R.D., and A.M.

Funding

This work was funded by SERB, Government of India, via EMR/2017/002324.

Notes

The authors declare no competing financial interest.

ACKNOWLEDGMENTS

The authors earnestly acknowledge SERB, Government of India, via EMR/2017/002324 for funding this work. They also thank IISER Kolkata for infrastructural and financial support. S.A. thanks UGC and M.M., M.P.C., and I.B. thank CSIR for providing the research fellowships. A.G. is grateful for the Early Career Research Award from the Department of Science and Technology, Govt. of India (ECR/2015/000220), and Wellcome Trust-DBT India Alliance Fellowship (IA/I/16/1/502369). R.D. sincerely acknowledges SERB for ECR/2015/000142 and DBT Ramalingaswami Fellowship (BT/RFF/R-entry/14/2014). We also thank Mr. Tamal Ghosh for helping us in flow cytometry analysis studies.

REFERENCES

(1) Jemal, A.; Bray, F.; Center Melissa, M.; Ferlay, J.; Ward, E.; Forman, D. Global cancer statistics. *Ca-Cancer J. Clin.* **2011**, *61*, 69−90.

(2) Oberoi, H. S.; Nukolova, N. V.; Kabanov, A. V.; Bronich, T. K. Nanocarriers for delivery of platinum anticancer drugs. *Adv. Drug Delivery Rev.* **2013**, *65*, 1667−1685.

(3) Florea, A.-M.; Buesselberg, D. Cisplatin as an anti-tumor drug: cellular mechanisms of activity, drug resistance and induced side effects. *Cancers* **2011**, *3*, 1351−1371.

(4) Kelland, L. The resurgence of platinum-based cancer chemotherapy. *Nat. Rev. Cancer* **2007**, *7*, 573−584.

(5) Johnstone, T. C.; Suntharalingam, K.; Lippard, S. J. The Next Generation of Platinum Drugs: Targeted Pt(II) Agents, Nanoparticle Delivery, and Pt(IV) Prodrugs. *Chem. Rev.* **2016**, *116*, 3436−3486.

(6) Tian, M.; Li, J.; Zhang, S.; Guo, L.; He, X.; Kong, D.; Zhang, H.; Liu, Z. Half-sandwich ruthenium(II) complexes containing NN̂-chelated imino-pyridyl ligands that are selectively toxic to cancer cells. *Chem. Commun.* **2017**, *53*, 12810−12813.

(7) Clarke, M. J.; Zhu, F.; Frasca, D. R. Non-Platinum Chemotherapeutic Metallopharmaceuticals. *Chem. Rev.* **1999**, *99*, 2511−2533.

(8) Kenny, R. G.; Marmion, C. J. Toward Multi-Targeted Platinum and Ruthenium Drugs-A New Paradigm in Cancer Drug Treatment Regimens? *Chem. Rev.* **2019**, *119*, 1058−1137.

(9) Anthony, E. J.; Bolitho, E. M.; Bridgewater, H. E.; Carter, O. W. L.; Donnelly, J. M.; Imberti, C.; Lant, E. C.; Lermyte, F.; Needham, R. J.; Palau, M.; Sadler, P. J.; Shi, H.; Wang, F.-X.; Zhang, W.-Y.; Zhang, Z. Metallodrugs are unique: opportunities and challenges of discovery and development. *Chem. Sci.* **2020**, *11*, 12888−12917.

(10) Zeng, L.; Gupta, P.; Chen, Y.; Wang, E.; Ji, L.; Chao, H.; Chen, Z.-S. The development of anticancer ruthenium(II) complexes: from single molecule compounds to nanomaterials. *Chem. Soc. Rev.* **2017**, *46*, 5771−5804.

(11) Meier-Menches, S. M.; Gerner, C.; Berger, W.; Hartinger, C. G.; Keppler, B. K. Structure-activity relationships for ruthenium and osmium anticancer agents - towards clinical development. *Chem. Soc. Rev.* **2018**, *47*, 909−928.

(12) Trondl, R.; Heffeter, P.; Kowol, C. R.; Jakupec, M. A.; Berger, W.; Keppler, B. K. NKP-1339, the first ruthenium-based anticancer drug on the edge to clinical application. *Chem. Sci.* **2014**, *5*, 2925−2932.

(13) Chitambar, C. R. Gallium-containing anticancer compounds. *Future Med. Chem.* **2012**, *4*, 1257−1272.

(14) Timerbaev, A. R. Advances in developing tris(8-quinolinolato)-gallium(III) as an anticancer drug: critical appraisal and prospects. *Metallomics* **2009**, *1*, 193−198.

(15) Thota, S.; Rodrigues, D. A.; Crans, D. C.; Barreiro, E. J. Ru(II) Compounds: Next-Generation Anticancer Metallotherapeutics? *J. Med. Chem.* **2018**, *61*, 5805−5821.

(16) Flocke, L. S.; Trondl, R.; Jakupec, M. A.; Keppler, B. K. Molecular mode of action of NKP-1339 - a clinically investigated

ruthenium-based drug - involves ER- and ROS-related effects in colon carcinoma cell lines. *Invest. New Drugs* **2016**, *34*, 261−268.
(17) Monro, S.; Colon, K. L.; Yin, H.; Roque, J.; Konda, P.; Gujar, S.; Thummel, R. P.; Lilge, L.; Cameron, C. G.; McFarland, S. A. Transition Metal Complexes and Photodynamic Therapy from a Tumor-Centered Approach: Challenges, Opportunities, and Highlights from the Development of TLD1433. *Chem. Rev.* **2019**, *119*, 797−828.
(18) Morris, R. E.; Aird, R. E.; Murdoch, P. d. S.; Chen, H.; Cummings, J.; Hughes, N. D.; Parsons, S.; Parkin, A.; Boyd, G.; Jodrell, D. I.; Sadler, P. J. Inhibition of Cancer Cell Growth by Ruthenium(II) Arene Complexes. *J. Med. Chem.* **2001**, *44*, 3616−3621.
(19) Nowak-Sliwinska, P.; van Beijnum, J. R.; Casini, A.; Nazarov, A. A.; Wagnieres, G.; van den Bergh, H.; Dyson, P. J.; Griffioen, A. W. Organometallic Ruthenium(II) Arene Compounds with Antiangiogenic Activity. *J. Med. Chem.* **2011**, *54*, 3895−3902.
(20) Chen, H.; Parkinson, J. A.; Parsons, S.; Coxall, R. A.; Gould, R. O.; Sadler, P. J. Organometallic Ruthenium(II) Diamine Anticancer Complexes: Arene-Nucleobase Stacking and Stereospecific Hydrogen-Bonding in Guanine Adducts. *J. Am. Chem. Soc.* **2002**, *124*, 3064−3082.
(21) Wang, F.; Habtemariam, A.; van der Geer, E. P. L.; Fernandez, R.; Melchart, M.; Deeth, R. J.; Aird, R.; Guichard, S.; Fabbiani, F. P. A.; Lozano-Casal, P.; Oswald, I. D. H.; Jodrell, D. I.; Parsons, S.; Sadler, P. J. Controlling ligand substitution reactions of organometallic complexes: Tuning cancer cell cytotoxicity. *Proc. Natl. Acad. Sci. U.S.A.* **2005**, *102*, 18269−18274.
(22) Bansal, P.; Lazo, J. S. Induction of Cdc25B Regulates Cell Cycle Resumption after Genotoxic Stress. *Cancer Res.* **2007**, *67*, 3356−3363.
(23) Ronconi, L.; Sadler, P. J. Using coordination chemistry to design new medicines. *Coord. Chem. Rev.* **2007**, *251*, 1633−1648.
(24) Maji, M.; Acharya, S.; Maji, S.; Purkait, K.; Gupta, A.; Mukherjee, A. Differences in Stability, Cytotoxicity, and Mechanism of Action of Ru(II) and Pt(II) Complexes of a Bidentate N,O Donor Ligand. *Inorg. Chem.* **2020**, *59*, 10262−10274.
(25) Chen, H.; Parkinson, J. A.; Morris, R. E.; Sadler, P. J. Highly Selective Binding of Organometallic Ruthenium Ethylenediamine Complexes to Nucleic Acids: Novel Recognition Mechanisms. *J. Am. Chem. Soc.* **2003**, *125*, 173−186.
(26) Mukherjee, A.; Acharya, S.; Purkait, K.; Chakraborty, K.; Bhattacharjee, A.; Mukherjee, A. Effect of N,N Coordination and RuII Halide Bond in Enhancing Selective Toxicity of a Tyramine-Based RuII (p-Cymene) Complex. *Inorg. Chem.* **2020**, *59*, 6581−6594.
(27) Romero-Canelón, I.; Salassa, L.; Sadler, P. J. The Contrasting Activity of Iodido versus Chlorido Ruthenium and Osmium Arene Azo- and Imino-pyridine Anticancer Complexes: Control of Cell Selectivity, Cross-Resistance, p53 Dependence, and Apoptosis Pathway. *J. Med. Chem.* **2013**, *56*, 1291−1300.
(28) Clavel, C. M.; Paunescu, E.; Nowak-Sliwinska, P.; Griffioen, A. W.; Scopelliti, R.; Dyson, P. J. Modulating the Anticancer Activity of Ruthenium(II)-Arene Complexes. *J. Med. Chem.* **2015**, *58*, 3356−3365.
(29) Griffith, D.; Morgan, M. P.; Marmion, C. J. A novel anti-cancer bifunctional platinum drug candidate with dual DNA binding and histone deacetylase inhibitory activity. *Chem. Commun.* **2009**, *12*, 6735−6737.
(30) Mandal, P.; Kundu, B. K.; Vyas, K.; Sabu, V.; Helen, A.; Dhankhar, S. S.; Nagaraja, C. M.; Bhattacherjee, D.; Bhabak, K. P.; Mukhopadhyay, S. Ruthenium(II) arene NSAID complexes: inhibition of cyclooxygenase and antiproliferative activity against cancer cell lines. *Dalton Trans.* **2018**, *47*, 517−527.
(31) Qiu, K.; Chen, Y.; Rees, T. W.; Ji, L.; Chao, H. Organelle-targeting metal complexes: From molecular design to bio-applications. *Coord. Chem. Rev.* **2019**, *378*, 66−86.
(32) Ramu, V.; Gautam, S.; Kondaiah, P.; Chakravarty, A. R. Diplatinum(II) Catecholate of Photoactive Boron-Dipyrromethene for Lysosome-Targeted Photodynamic Therapy in Red Light. *Inorg. Chem.* **2019**, *58*, 9067−9075.
(33) Wong, D. Y. Q.; Lim, J. H.; Ang, W. H. Induction of targeted necrosis with HER2-targeted platinum(IV) anticancer prodrugs. *Chem. Sci.* **2015**, *6*, 3051−3056.
(34) Patra, M.; Awuah, S. G.; Lippard, S. J. Chemical Approach to Positional Isomers of Glucose-Platinum Conjugates Reveals Specific Cancer Targeting through Glucose-Transporter-Mediated Uptake in Vitro and in Vivo. *J. Am. Chem. Soc.* **2016**, *138*, 12541−12551.
(35) Bhattacharyya, S.; Purkait, K.; Mukherjee, A. Ruthenium(II) p-cymene complexes of a benzimidazole-based ligand capable of VEGFR2 inhibition: hydrolysis, reactivity and cytotoxicity studies. *Dalton Trans.* **2017**, *46*, 8539−8554.
(36) Liu, X.; Zhang, L.-L.; Xu, X.-H.; Hui, L.; Zhang, J.-B.; Chen, S.-W. Synthesis and anticancer activity of dichloroplatinum(II) complexes of podophyllotoxin. *Bioorg. Med. Chem. Lett.* **2013**, *23*, 3780−3784.
(37) Vock, C. A.; Ang, W. H.; Scolaro, C.; Phillips, A. D.; Lagopoulos, L.; Juillerat-Jeanneret, L.; Sava, G.; Scopelliti, R.; Dyson, P. J. Development of Ruthenium Antitumor Drugs that Overcome Multidrug Resistance Mechanisms. *J. Med. Chem.* **2007**, *50*, 2166−2175.
(38) Acharya, S.; Ghosh, S.; Maji, M.; Parambil, A. R. U.; Singh, S.; Mukherjee, A. Inhibition of 3D colon cancer stem cell spheroids by cytotoxic RuII-p-cymene complexes of mesalazine derivatives. *Chem. Commun.* **2020**, *56*, 5421−5424.
(39) Zajac, J.; Novohradsky, V.; Markova, L.; Brabec, V.; Kasparkova, J. Platinum (IV) Derivatives with Cinnamate Axial Ligands as Potent Agents Against Both Differentiated and Tumorigenic Cancer Stem Rhabdomyosarcoma Cells. *Angew. Chem., Int. Ed.* **2020**, *59*, 3329−3335.
(40) Acharya, S.; Maji, M.; Ruturaj; Purkait, K.; Gupta, A.; Mukherjee, A. Synthesis, Structure, Stability, and Inhibition of Tubulin Polymerization by Ru(II)-p-Cymene Complexes of Trimethoxyaniline-Based Schiff Bases. *Inorg. Chem.* **2019**, *58*, 9213−9224.
(41) Dogterom, M.; Koenderink, G. H. Actin-microtubule crosstalk in cell biology. *Nat. Rev. Mol. Cell Biol.* **2019**, *20*, 38−54.
(42) Huang, X.; Huang, R.; Gou, S.; Wang, Z.; Liao, Z.; Wang, H. Combretastatin A-4 Analogue: A Dual-Targeting and Tubulin Inhibitor Containing Antitumor Pt(IV) Moiety with a Unique Mode of Action. *Bioconjugate Chem.* **2016**, *27*, 2132−2148.
(43) Huang, X.; Huang, R.; Gou, S.; Wang, Z.; Liao, Z.; Wang, H. Platinum(IV) complexes conjugated with phenstatin analogue as inhibitors of microtubule polymerization and reverser of multidrug resistance. *Bioorg. Med. Chem.* **2017**, *25*, 4686−4700.
(44) Huang, X.; Huang, R.; Wang, Z.; Li, L.; Gou, S.; Liao, Z.; Wang, H. Pt(IV) complexes conjugating with chalcone analogue as inhibitors of microtubule polymerization exhibited selective inhibition in human cancer cells. *Eur. J. Med. Chem.* **2018**, *146*, 435−450.
(45) Huang, X.; Hua, S.; Huang, R.; Liu, Z.; Gou, S.; Wang, Z.; Liao, Z.; Wang, H. Dual-targeting antitumor hybrids derived from Pt(IV) species and millepachine analogues. *Eur. J. Med. Chem.* **2018**, *148*, 1−25.
(46) Fu, Y.; Sanchez-Cano, C.; Soni, R.; Romero-Canelon, I.; Hearn, J. M.; Liu, Z.; Wills, M.; Sadler, P. J. The contrasting catalytic efficiency and cancer cell antiproliferative activity of stereoselective organoruthenium transfer hydrogenation catalysts. *Dalton Trans.* **2016**, *45*, 8367−8378.
(47) van Rixel, V. H. S.; Ramu, V.; Auyeung, A. B.; Beztsinna, N.; Leger, D. Y.; Lameijer, L. N.; Hilt, S. T.; Le Devedec, S. E.; Yildiz, T.; Betancourt, T.; Gildner, M. B.; Hudnall, T. W.; Sol, V.; Liagre, B.; Kornienko, A.; Bonnet, S. Photo-Uncaging of a Microtubule-Targeted Rigidin Analogue in Hypoxic Cancer Cells and in a Xenograft Mouse Model. *J. Am. Chem. Soc.* **2019**, *141*, 18444−18454.
(48) Pasquier, E.; Honore, S.; Braguer, D. Microtubule-targeting agents in angiogenesis: where do we stand? *Drug Resist. Updates* **2006**, *9*, 74−86.
(49) Su, M.; Huang, J.; Liu, S.; Xiao, Y.; Qin, X.; Liu, J.; Pi, C.; Luo, T.; Li, J.; Chen, X.; Luo, Z. The anti-angiogenic effect and novel mechanisms of action of Combretastatin A-4. *Sci. Rep.* **2016**, *6*, No. 28139.

https://dx.doi.org/10.1021/acs.inorgchem.0c03820
Inorg. Chem. 2021, 60, 3418−3430

(50) Meissner, M.; Pinter, A.; Michailidou, D.; Hrgovic, I.; Kaprolat, N.; Stein, M.; Holtmeier, W.; Kaufmann, R.; Gille, J. Microtubule-Targeted Drugs Inhibit VEGF Receptor-2 Expression by both Transcriptional and Post-Transcriptional Mechanisms. *J. Invest. Dermatol.* **2008**, *128*, 2084−2091.
(51) Koch, S.; Claesson-Welsh, L. Signal transduction by vascular endothelial growth factor receptors. *Cold Spring Harbor Perspect. Med.* **2012**, *2*, No. a006502.
(52) Czeisler, C.; Mikawa, T. Microtubules coordinate VEGFR2 signaling and sorting. *PLoS One* **2013**, *8*, No. e75833.
(53) Kukushkin, V. Y.; Pombeiro, A. J. L.; Ferreira, C. M. P.; Elding, L. I.; Puddephatt, R. J. Compounds of general interest. Dimethylsulfoxide complexes of platinum(II): K[PtCl3(Me2SO)], cis-[PtCl2L-(Me2SO)] (L = Me2SO, MeCN), [PtCl(μ-Cl)(Me2SO)]2, and [Pt(Me2SO)4](CF3SO3)2. *Inorg. Synth.* **2002**, *33*, 189−196.
(54) Bennett, M. A.; Huang, T. N.; Matheson, T. W.; Smith, A. K. (η6-Hexamethylbenzene)ruthenium complexes. *Inorg. Synth.* **1982**, *21*, 74−78.
(55) Hall, M. D.; Telma, K. A.; Chang, K.-E.; Lee, T. D.; Madigan, J. P.; Lloyd, J. R.; Goldlust, I. S.; Hoeschele, J. D.; Gottesman, M. M. Say No to DMSO: Dimethylsulfoxide Inactivates Cisplatin, Carboplatin, and Other Platinum Complexes. *Cancer Res.* **2014**, *74*, 3913−3922.
(56) Backler, F.; Wilson, G. J.; Wang, F. Rational use of ligand to shift the UV−vis spectrum of Ru-complex sensitiser dyes for DSSC applications. *Radiat. Phys. Chem.* **2019**, *161*, 66−71.
(57) Kumar, K. N.; Venkatachalam, G.; Ramesh, R.; Liu, Y. Half-sandwich para-cymene ruthenium(II) naphthylazophenolato complexes: Synthesis, molecular structure, light emission, redox behavior and catalytic oxidation properties. *Polyhedron* **2008**, *27*, 157−166.
(58) Pizarro, A. M.; Habtemariam, A.; Sadler, P. J. Activation mechanisms for organometallic anticancer complexes. In *Medicinal Organometallic Chemistry*; Topics in Organometallic Chemistry; Springer: Berlin, Heidelberg, 2010; Vol *32*, pp 21−56.
(59) Kubanik, M.; Holtkamp, H.; Sohnel, T.; Jamieson, S. M. F.; Hartinger, C. G. Impact of the Halogen Substitution Pattern on the Biological Activity of Organoruthenium 8-Hydroxyquinoline Anticancer Agents. *Organometallics* **2015**, *34*, 5658−5668.
(60) Biancalana, L.; Abdalghani, I.; Chiellini, F.; Zacchini, S.; Pampaloni, G.; Crucianelli, M.; Marchetti, F. Ruthenium Arene Complexes with α-Aminoacidato Ligands: New Insights into Transfer Hydrogenation Reactions and Cytotoxic Behaviour. *Eur. J. Inorg. Chem.* **2018**, *2018*, 3041−3057.
(61) Reithofer, M. R.; Bytzek, A. K.; Valiahdi, S. M.; Kowol, C. R.; Groessl, M.; Hartinger, C. G.; Jakupec, M. A.; Galanski, M.; Keppler, B. K. Tuning of lipophilicity and cytotoxic potency by structural variation of anticancer platinum(IV) complexes. *J. Inorg. Biochem.* **2011**, *105*, 46−51.
(62) Hansch, C.; Maloney, P. P.; Fujita, T.; Muir, R. M. Correlation of biological activity of phenoxyacetic acids with Hammett substituent constants and partition coefficients. *Nature* **1962**, *194*, 178−180.
(63) Ruiz, J.; Rodriguez, V.; Cutillas, N.; Espinosa, A.; Hannon, M. J. A Potent Ruthenium(II) Antitumor Complex Bearing a Lipophilic Levonorgestrel Group. *Inorg. Chem.* **2011**, *50*, 9164−9171.
(64) Mendoza-Ferri, M.-G.; Hartinger, C. G.; Eichinger, R. E.; Stolyarova, N.; Severin, K.; Jakupec, M. A.; Nazarov, A. A.; Keppler, B. K. Influence of the Spacer Length on the in Vitro Anticancer Activity of Dinuclear Ruthenium-Arene Compounds. *Organometallics* **2008**, *27*, 2405−2407.
(65) Maji, M.; Karmakar, S.; Ruturaj; Gupta, A.; Mukherjee, A. Oxamusplatin: a cytotoxic Pt(II) complex of a nitrogen mustard with resistance to thiol based sequestration displays enhanced selectivity towards cancer. *Dalton Trans.* **2020**, *49*, 2547−2558.
(66) Oliveira, K. M.; Peterson, E. J.; Carroccia, M. C.; Cominetti, M. R.; Deflon, V. M.; Farrell, N. P.; Batista, A. A.; Correa, R. S. Ru(II)-Naphthoquinone complexes with high selectivity for triple-negative breast cancer. *Dalton Trans.* **2020**, *49*, 16193−16203.
(67) Morone, N.; Fujiwara, T.; Murase, K.; Kasai, R. S.; Ike, H.; Yuasa, S.; Usukura, J.; Kusumi, A. Three-dimensional reconstruction of the membrane skeleton at the plasma membrane interface by electron tomography. *J. Cell Biol.* **2006**, *174*, 851−862.
(68) Casaletto, J. B.; McClatchey, A. I. Spatial regulation of receptor tyrosine kinases in development and cancer. *Nat. Rev. Cancer* **2012**, *12*, 387−400.
(69) Chung, I.; Akita, R.; Vandlen, R.; Toomre, D.; Schlessinger, J.; Mellman, I. Spatial control of EGF receptor activation by reversible dimerization on living cells. *Nature* **2010**, *464*, 783−787.
(70) FIELD Authors: Bayless, K. J.; Johnson, G. A. Role of the cytoskeleton in formation and maintenance of angiogenic sprouts. *J. Vasc. Res.* **2011**, *48*, 369−385.
(71) Simons, M.; Gordon, E.; Claesson-Welsh, L. Mechanisms and regulation of endothelial VEGF receptor signalling. *Nat. Rev. Mol. Cell Biol.* **2016**, *17*, 611−625.
(72) Sase, H.; Watabe, T.; Kawasaki, K.; Miyazono, K.; Miyazawa, K. VEGFR2-PLCγ1 axis is essential for endothelial specification of VEGFR2+ vascular progenitor cells. *J. Cell Sci.* **2009**, *122*, 3303−3311.
(73) Sitati, M. K.; Jaganyi, D.; Mambanda, A. The rate of substitution from η6-arene ruthenium(II) complexes. *Transition Met. Chem.* **2020**, *45*, 305−315.

https://dx.doi.org/10.1021/acs.inorgchem.0c03820
Inorg. Chem. 2021, 60, 3418−3430